

## Article

# Structure and Electrical Properties of Carbon-Rich Polymer Derived Silicon Carbonitride (SiCN)

Oluwole Daniel Adigun <sup>1,2,3,\*</sup> , Emmanuel Ricohermoso III <sup>2</sup> , Ayodele Abeeb Daniyan <sup>1</sup>,  
Lasisi Ejibunu Umoru <sup>1</sup> and Emanuel Ionescu <sup>2,4</sup> 

<sup>1</sup> Department of Materials Science and Engineering, Obafemi Awolowo University, Ile Ife 220101, Nigeria

<sup>2</sup> Fachbereich Material-Und Geowissenschaften, Technische Universität Darmstadt, 64287 Darmstadt, Germany

<sup>3</sup> Department of Metallurgical and Materials Engineering, Federal University Oye, Oye-Ekiti 370111, Nigeria

<sup>4</sup> Fraunhofer IWKS, Department Digitalization of Resources, Brentanost. 2a, 63755 Alzenau, Germany

\* Correspondence: oluwole.adigun@fuoye.edu.ng

**Abstract:** This article reports on the structure and electronic properties of carbon-rich polysilazane polymer-derived silicon carbonitride (C/SiCN) corresponding to pyrolysis temperatures between 1100 and 1600 °C in an argon atmosphere. Raman spectroscopy, X-ray diffraction (XRD), energy dispersive X-ray spectroscopy (EDX), Scanning Electron Microscopy (SEM) and Hall measurements were used to support the structural and electronic properties characterization of the prepared C/SiCN nanocomposites. A structural analysis using Raman spectroscopy showed the evolution of sp<sup>2</sup> hybridized carbon phase that resulted from the growth in the lateral crystallite size (L<sub>a</sub>), average continuous graphene length including tortuosity (L<sub>eq</sub>) and inter-defects distance (L<sub>D</sub>) with an increase in pyrolysis temperature. The prepared C/SiCN monoliths showed a record high room temperature (RT) electrical conductivity of 9.6 S/cm for the sample prepared at 1600 °C. The electronic properties of the nanocomposites determined using Hall measurement revealed an anomalous change in the predominant charge carriers from n-type in the samples pyrolyzed at 1100 °C to predominantly p-type in the samples prepared at 1400 and 1600 °C. According to this outcome, tailor-made carbon-rich SiCN polymer-derived ceramics could be developed to produce n-type and p-type semiconductors for development of the next generation of electronic systems for applications in extreme temperature environments.

**Keywords:** Polymer derived ceramics (PDC); silicon carbonitride (SiCN); semiconductor; free/sp<sup>2</sup>-hybridized carbon; nanocomposite



**Citation:** Adigun, O.D.; Ricohermoso, E., III; Daniyan, A.A.; Umoru, L.E.; Ionescu, E. Structure and Electrical Properties of Carbon-Rich Polymer Derived Silicon Carbonitride (SiCN). *Ceramics* **2022**, *5*, 690–705. <https://doi.org/10.3390/ceramics5040050>

Academic Editor: John W. Halloran

Received: 25 August 2022

Accepted: 27 September 2022

Published: 3 October 2022

**Publisher's Note:** MDPI stays neutral with regard to jurisdictional claims in published maps and institutional affiliations.



**Copyright:** © 2022 by the authors. Licensee MDPI, Basel, Switzerland. This article is an open access article distributed under the terms and conditions of the Creative Commons Attribution (CC BY) license (<https://creativecommons.org/licenses/by/4.0/>).

## 1. Introduction

Broad studies on the electrical properties of polymer-derived ceramics (also called PDCs, e.g., SiC, SiCN, SiOCN, SiOC, etc.) and their composites have been on the rise in recent years [1,2]. Motivation for such extensive studies is centered on the tailorability of their structure, easy shaping processes and their functional applications, particularly in the area of semiconductor-based electronic systems such as micro-electromechanical systems (MEMS) and microsensors for applications in high-temperature environments [3–5]. These materials have demonstrated features that announce properties already known for conventional silicon-based semiconductors and have equally shown unique properties beyond what was previously achievable. Among these classes of semiconducting ceramic materials, the non-oxide silicon carbonitrides (SiCN), have shown both higher temperature stability in terms of oxidation and creep resistance ( $\geq 1600$  °C) and wider band gap (at room temperature) over others [6–9].

While amorphous Si-C-N produced by the pyrolysis of polysilazane at a temperature  $< 1200$  °C in inert atmosphere is made up of a single Si<sub>x</sub>C<sub>y</sub>N<sub>z</sub> phase and free carbon, the crystalline state pyrolyzed beyond  $\sim 1350$  °C comprises of SiC, Si<sub>3</sub>N<sub>4</sub> and C nanocomposite phases (C is free carbon; also called sp<sup>2</sup> hybridized carbon, turbostratic carbon or graphitic

carbon) [10–12]. The amorphous phase is associated with very low electrical conductivity ( $\sigma_{dc}$ ), in the range of  $10^{-9}$  to  $10^{-2}$  S/cm, but a vast increase of several orders of magnitude is observed as the material transforms to crystalline state via increase in pyrolysis temperature [13,14]. Over the years, the strong increase in room temperature (RT) conductivity has been attributed to increase in pyrolysis temperature during thermal treatment of the material, which in turn leads to the following: (i) structural transformation of the carbon phase from amorphous carbon to ordered  $sp^2$ -hybridized carbon (Note that the RT conductivity of  $sp^2$  hybridized carbon is  $10^0$  to  $10^5$  S/cm); (ii) crystallization of  $\beta$ -SiC (Note that only SiC and  $sp^2$ -hybridized carbon are semiconductors in the composition,  $Si_3N_4$  is an insulator and does not contribute to conductivity); and (iii) Nitrogen (N) doping of the  $\beta$ -SiC as  $Si_3N_4$  (in the SiC/ $Si_3N_4$ /C nanocomposite) decomposes gradually to give off  $N_2$  gas at higher temperatures when  $T > \sim 1400$  °C [9,15]. While these assertions have been proven and corroborated by various characterization techniques such as XANES spectroscopy, XRD, TEM and Raman Spectroscopy, a profound understanding of the electrical conductivity of SiCN PDCs, particularly the charge carrier transport mechanisms, remain incomplete. Seeing the emerging potential of SiCN as semiconductor materials for the next generation of electronics for applications in extreme temperature environments, developing an understanding of the carrier transport mechanism is important in order to study the principle leading to its electrical conductivity as this could aid in their fabrication for various useful electronic purposes.

Evaluation of the electrical conductivity of polysilazane-derived SiCN began in the early 90s with the work of Mocaer but studies on their charge carrier transport are still very rare to come by in the literature [16,17]. One of the ways to determine carrier mobility ( $\mu_H$ ), carrier type (n-type or p-type), carrier density/concentration ( $N$ ), conductivity ( $\sigma_{dc}$ ) and other useful electrical conductivity parameters in a semiconductor is through Hall measurement. The principle and efficiency of Hall measurement technique for the assessment of semiconductivity in shaped crystal articles and thin films have been emphasized [18,19]. Usually, semiconductor materials either possess a majority positive or negative charge carriers signifying p-type or n-type semiconductors, respectively. However, some materials appear to have played out the two charge carrier types as majority carriers at the same time under different conditions. In a recent study aimed at characterizing the electrical properties of SiCN(O) PDCs, Ryu et al. revealed that some samples gave both positive and negative signs of Hall coefficient, but it could not be inferred as to whether the samples were of p-type or n-type semiconductors [16].

Similarly, the question of why a single material possesses both positive and negative Hall coefficient (i.e., both n and p-type majority charge carriers) is still a subject of unresolved debate [20,21]. The compositions, processing conditions, and the nanostructure of the materials could be the intrinsic source of these observations. For instance, after assessing the effect of thermal treatments on the electrical conductivity of SiCN and SiBCN ceramics, Hermann et al. recently reported that addition of boron increased the on-set crystallization temperature of SiCN PDC because boron retarded the atomic mobility, and the Si(B)CN ceramic showed higher RT conductivity than the as-pyrolyzed SiCN ceramics [22]. Besides the use of metal addition to improve electrical properties, conscious formation of  $sp^2$  hybridized carbon phases by raising the carbon content can also help increase electrical properties of PDCs. This can be achieved via custom-made precursor synthesis [23], mixing of different commercially available precursors [24] or direct addition of a suitable crosslinker [25,26]. Among these approaches, it is the direct addition of a suitable cross-linker that is the most straightforward and easy. Divinylbenzene (DVB) is a common cross-linking agent used to adjust the resulting chemical and structural composition of PDCs by increasing the carbon content and molecular weight/ceramic yield [27]. The resulting formation of  $sp^2$  hybridized carbon phase from the rise in carbon content has been shown to be beneficial to electrical properties [26,28]. The type of the inert atmosphere adopted during thermal treatment has also been identified as a crucial factor that determines electrical conductivity behaviour via carbothermic composition adjustments [9].

In [9], Haluschka et al. investigated the influence of ammonia (NH<sub>3</sub>) alone and argon (Ar)/ammonia gas mixture atmosphere on thermally induced RT conductivity of SiCN and reported that free carbon content of the materials is reduced due to enhanced methane evolution in the ammonia (NH<sub>3</sub>) atmosphere, resulting in a progressive replacement of carbon by nitrogen and this led to decrease in RT electrical conductivity by up to 4 orders of magnitude. Consequently, the electrical conductivity of semiconductor engineering ceramics can also be modified through the choice of pyrolysis atmosphere. So far, some applications of electrically conducting carbon rich PDCs where tailoring the chemical composition could influence the properties of the ceramics and make them of functional use have been displayed in batteries or electrocatalysis [29–31]. Motivated by the exceptional properties of carbon rich PDCs that have evolved in the recent past and the high temperatures stability of SiCN PDCs, it is believed that a tailor-made chemical composition of carbon rich SiCN could hold prospects for novel discoveries in other application areas such as thermopower or high temperature electronics that requires basically p-type and n-type semiconductors. Moreover, investigation of the ordering of the sp<sup>2</sup>-hybridized free carbon phase in SiOC/C PDCs via thermal treatment reported by Rosenberg et al. [24] could be replicated in the carbon rich SiCN systems for the extraction of innovative information, and this is where the current study comes in.

Here we present the electrical properties of carbon-rich SiCN (up to ca. 72 at. % carbon) with attention to the observed anomalous shift in the dominant charge carriers from n-type in the amorphous glassy matrix pyrolyzed at 1100 °C to mainly p-type in the crystalline ceramic samples prepared at 1400–1600 °C. Such resulting technical ceramics could be of great interest for the development of semiconductors applied in harsh environments. The amount, size and evolution of the sp<sup>2</sup>-hybridized free carbon phase with the thermal treatment in an argon atmosphere as well as the charge carrier transport mechanism are characterized using Raman spectroscopy, Energy Dispersive X-ray Spectroscopy, EDX attached to a (High Resolution) Scanning Electron Microscopy –SEM, X-ray diffraction (XRD) and Hall measurements. The produced C/SiCN materials also show RT electrical conductivity (0.148–9.26 S/cm) that are quite higher than previously reported values for monolith samples produced using similar pyrolysis temperatures. Consequently, depending on the processing and the final chemical composition, C-rich SiCN PDCs may be tailored to produce n-type and p-type semiconductors for the development of the next generation of micro-electromechanical systems (MEMS) and other microelectronic devices for applications in extremely high temperature environments.

## 2. Experimental Procedures

### 2.1. Synthesis

Commercially available Durazane 1800 (Merck KGaA, Darmstadt, Germany) was used as the primary polysilazane polymer for the fabrication of the carbon-rich SiCN samples with 50 wt% Divinylbenzene, DVB (Sigma-Aldrich, subsidiary of Merck KGaA, Darmstadt, Germany) as a crosslinking agent in the presence of Platinum divinyl-tetramethyl disiloxane complex, ~Pt 2% in xylene (Sigma-Aldrich, subsidiary of Merck KGaA, Darmstadt, Germany) diluted to 0.1%, as catalyst. The composition was thoroughly stirred with a magnetic stirrer for 6 h at 120 °C for the hydrosilylation reaction which was done using standard Schlenk techniques in an argon atmosphere. All through the synthesis, the composition was appropriately confined under an argon atmosphere and thoroughly degassed at each point in vacuum to eliminate any dissolved impurities -due to the sensitivity of polysilazane towards oxygen and humidity. The composition was cross-linked at 250 °C for 3 h in an argon atmosphere to obtain an infusible preceramic solid which was ground for 2 h in a milling machine (Mixer Mill MM400, Retsch, Germany) to obtain very fine powder of about 40 μm. Approximately 200 mg of the preceramic powder was consolidated in a Ø 10 mm die using a warm press at 250 °C and 18 kN to form a green body. Consequently, the green body was pyrolyzed at 1100 °C and annealed at 1400 °C ≤ T ≤ 1600 °C in

an argon atmosphere to obtain C/SiCN nanocomposite monoliths. Additional descriptions of polysilazane monolith fabrication processes are reported in the literature [32,33].

## 2.2. Characterization

The elemental composition was determined using Energy Dispersive X-ray Spectroscopy, EDX, attached to a (High Resolution) Scanning Electron Microscopy, SEM (Philips XL30 FEG, Phillips, Hillsboro, OR, USA) while the morphology characterization was done using the SEM images. Crystallization of the C/SiCN powders was investigated using X-ray diffraction (XRD) in the transmission mode by STOE STAD1 P (STOE & Cie. GmbH, STOE, Darmstadt, Germany) using monochromatic Mo K $\alpha$  radiation at 0.1°/step with 25 s acquisition time for each step in the 2 $\theta$  range of 5–45°; consequently, the samples were investigated with a D8 Advance diffractometer (Bruker AXS GmbH, Karlsruhe, Germany) with Cu K $\alpha$  radiation in a reflection mode. The sp<sup>2</sup>-hybridized carbon phase was analysed using Raman spectroscopy (HR Raman Spectroscopy HR800, Horiba Jobin Yvon GmbH, Bensheim, Germany). The electrical conductivity and Hall measurements were investigated using the Van der Pauw method as described in [34].

## 3. Results and Discussion

### 3.1. Investigation of the Carbon Phase

Previous studies have shown that polysilazane-derived amorphous SiCN ceramics pyrolyzed at 900–1100 °C consist of mixed Si<sub>x</sub>C<sub>y</sub>N<sub>z</sub> bond and free carbon [35]. At a higher ceramization temperature (above ~1350 °C), however, the microstructure evolves into crystalline nanodomains made up of SiC, Si<sub>3</sub>N<sub>4</sub> and C with the sp<sup>2</sup> hybridized carbon phase playing a major role in influencing the functional properties of the SiCN material [35–37].

The microstructural evolution of the sp<sup>2</sup> hybridized carbon phase in the prepared carbon-rich SiCN samples was investigated using Raman Spectroscopy. The primary signals of the Raman spectra showing the carbon phase are the D and G bands identified at ~1350 cm<sup>-1</sup> and ~1582 cm<sup>-1</sup>, respectively, for the monoliths (see Figure 1a–c), but the secondary signals include prominent overtones and combination bands which are the 2D (or G'), 2D', T + D and D + G bands in the range of ~2500–3250 cm<sup>-1</sup> [38,39]. A D' band (at ~1500 cm<sup>-1</sup>) and T (~1200 cm<sup>-1</sup>) band which relate to amorphous carbon fractions and sp<sup>2</sup>-sp<sup>3</sup> C-C/C=C bonds respectively revealed in the monoliths are other two crucial bands that often stretch from the G and D band shoulders most especially shown in amorphous materials. The D' and T bands are prominent in the amorphous SiCN monolith samples produced at the pyrolysis temperature of 1100 °C. In the sample annealed at 1600 °C, a signal at ca. 820 cm<sup>-1</sup> was identified and assigned to  $\beta$ -SiC. In general, the peak position, width, intensities and overlapping Raman spectra give useful details on the structural evolution, defects and crystallite size of the graphitic carbon phase. The D band is a defect-prompted band that results due to a corresponding disorder (amorphization) from carbon nanostructure while the G band is formed by the internal stretching of highly ordered sp<sup>2</sup> hybridized carbon lattice [9,40,41]. At the temperature of 1100 °C, the D and G bands of the samples are seen to overlap which complicates separation of the profiles but at a temperature of  $\geq 1400$  °C, overlapping of the D and G bands has been greatly reduced (see Figure 1a–c). Moreover, Lorentzian fitting of the Raman bands was performed in order to extract information about the structural evolution of the carbon phase at elevated temperatures; and the rising intensities of the 2D band noticed in the prepared samples with an increase in temperature from 1100 °C to 1600 °C is an important indicator of the rising crystallinities of the graphitic nanostructure.

The lateral size of sp<sup>2</sup> hybridized carbon, L<sub>a</sub>, used to characterize the width of the graphitic crystallite of the samples along the a-axis, was determined using Equation (1) [42–44]. Where A<sub>D</sub>/A<sub>G</sub> is integrated intensities ratio of the D and G bands and  $\lambda$  is the laser line wavelength (514 nm).

$$L_a = (2.4 \times 10^{-10}) \lambda_L^4 \left( \frac{A_D}{A_G} \right)^{-1} \quad (1)$$

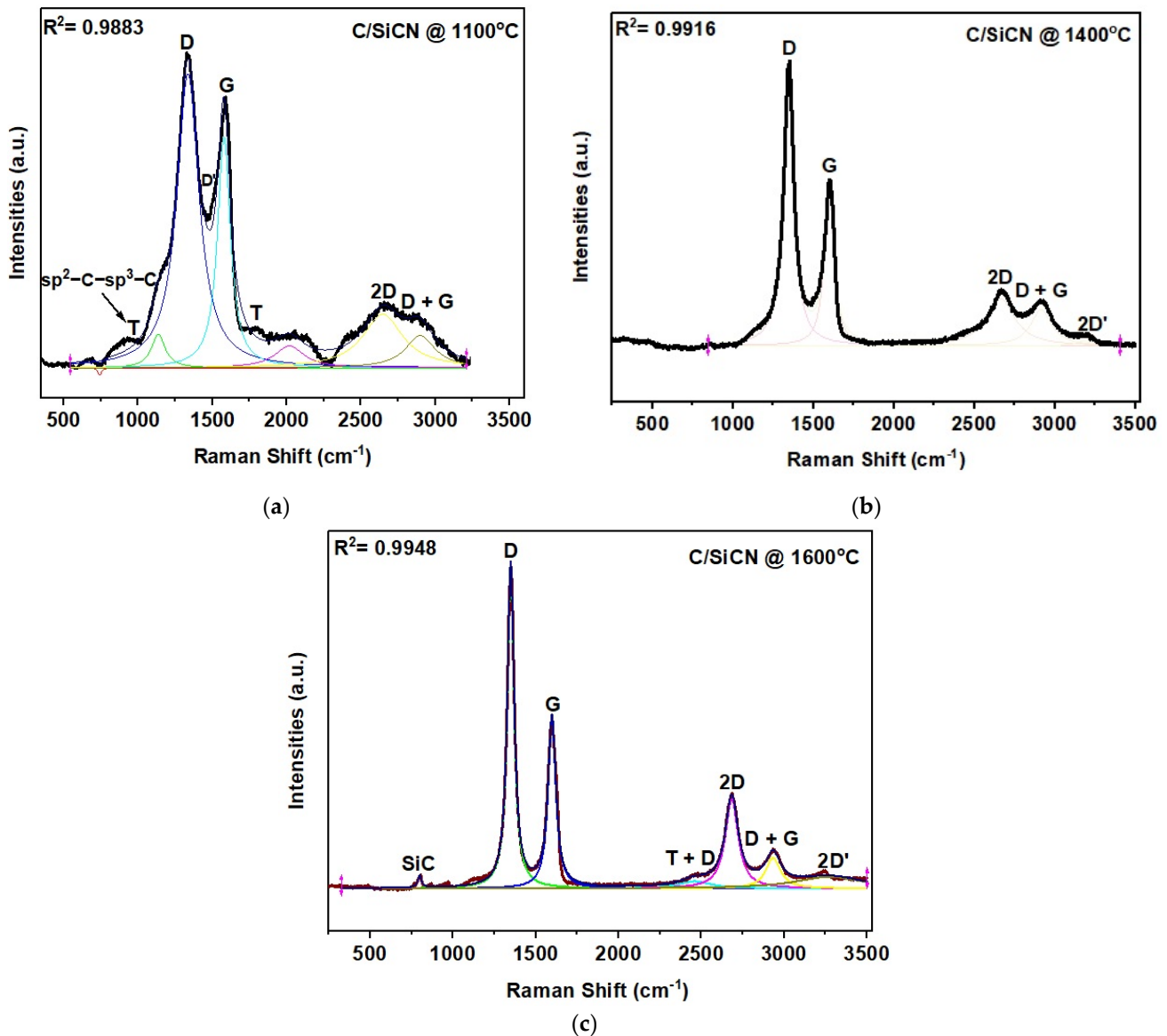


**Figure 1.** Raman spectra of the C/SiCN nanocomposites showing the carbon phase of various samples represented by the peak position and band parameters: (a) Raman spectrum of the amorphous C/SiCN nanocomposite pyrolyzed at 1100 °C; (b) Raman spectrum of the C/SiCN nanocomposite annealed at 1400 °C; (c) Raman spectrum of the C/SiCN nanocomposite annealed at 1600 °C.

The consistency of the integrated intensities ratio and its importance in the observation of the quantum Hall effect in graphitic materials for the design and fabrication of target electronic systems have been discussed in various studies [42,43,45]. The dependence of the lateral crystal size,  $L_a$ , of the graphitic nanostructure of the samples on the integrated intensities of the D and G bands, as well as its reliance on the thermal treatment, is presented in Figure 2a. The crystallite size,  $L_a$ , increased as the annealing temperatures used in making the samples increased between 1100 °C and 1600 °C.  $L_a$  reveals the width of a single  $sp^2$  hybridized carbon crystal unit and analysis of the Raman spectra shows that during the thermal processing, smaller crystallites grow to form larger size with higher degree of structural orderliness. This increase in crystallite size could be linked to kinetics generated within the materials during the annealing process. At 1600 °C, the crystallite size of the graphitic carbon has grown to ca. 10 nm (from ca. 7.7 nm at 1100 °C, see Figure 2a). Moreover, a recorded increase in  $L_a$  as a result of increased ceramization temperatures conforms with the work of Ricohermoso et al. as well as Rosenberg et al.,

who both studied the evolution of the  $sp^2$ -hybridized carbon phase in polymer-derived SiOC ceramics [24,46]. An improvement in the structural stability of a graphitic material in terms of strength and ductility could also be achieved via nucleation of the  $sp^2$  carbon crystallite size as discussed in a recent study [47]. In the same vein, Tarhini et al. revealed that a lateral crystallite size,  $L_a$ , greater than 7 nm led to improvements in in-plane electrical conductivity, thermal conductivity and tensile strength [48]. Therefore, an increase in  $L_a$  with temperature increases indicate corresponding growth in the degree of graphitization in the monoliths. On the other hand, as the degree of graphitization rises, the G band gains prominence over the defect-prompted D band, resulting in a decline of the integrated ratio of the D and G band with increasing the annealing temperature (see Figure 2a).

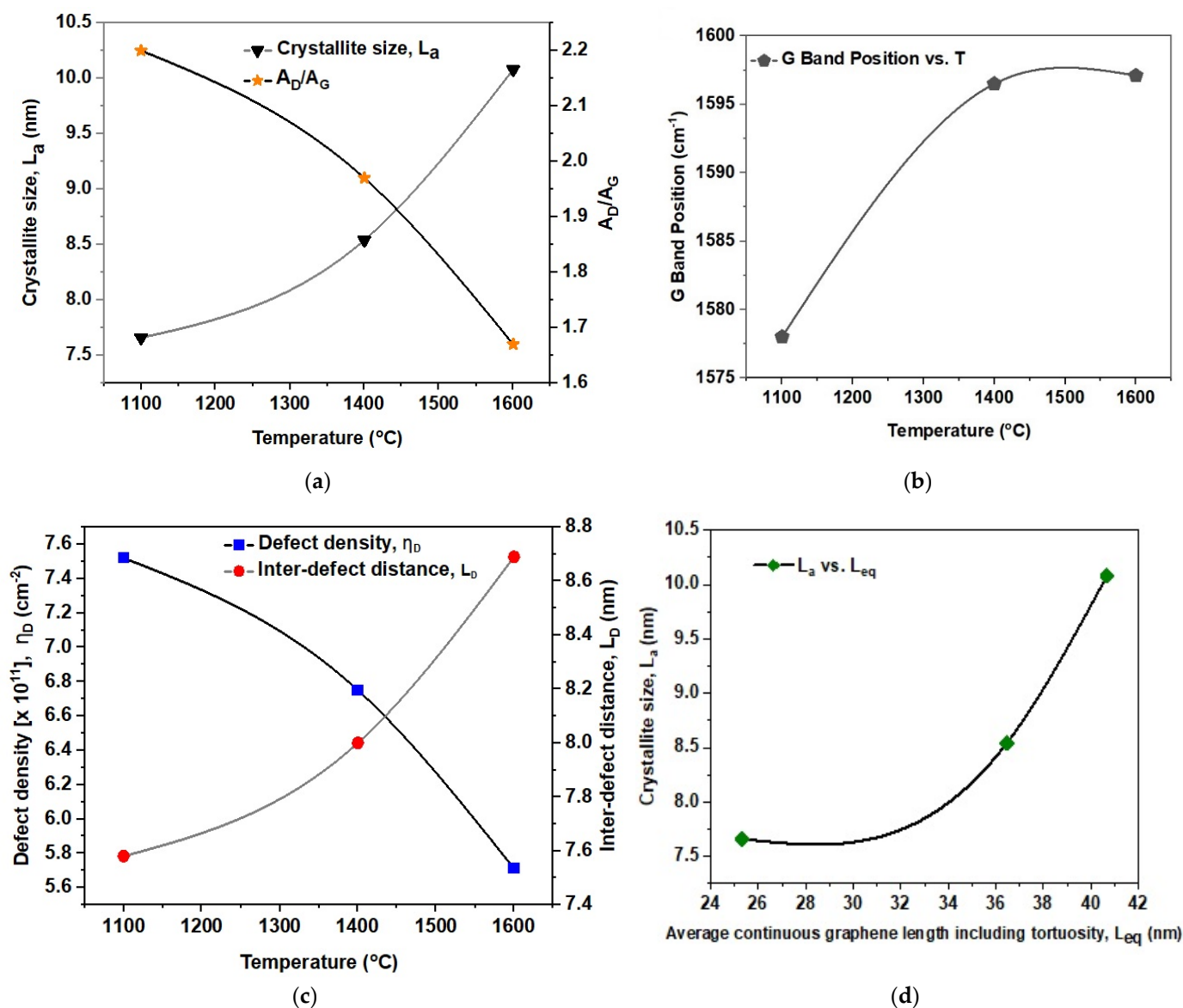


**Figure 2.** Parameters from Raman spectroscopy which determine the evolution of the  $sp^2$  hybridized carbon phase in the polymer-derived C/SiCN nanocomposite materials: (a) Dependence of crystallite size ( $L_a$ ) and integrated ratios of the D and G bands on temperature; (b) shift of the G band as a function of the pyrolysis temperature; (c) effect of ceramization temperatures on inter-defect distance ( $L_D$ ) and defect density ( $\eta_D$ ); (d) growth in crystallite size ( $L_a$ ) of the  $sp^2$  hybridized carbon with an increase in average continuous graphene length including tortuosity ( $L_{eq}$ ).

The margin of G band peak position shift between the fabrication temperatures of 1100 °C and 1400 °C is observed to be much higher than the shift interval noticed from 1400 °C to 1600 °C (see Figure 2b), indicating a high crystallization rate between 1100 °C and 1400 °C and slow ceramization between 1400 °C and 1600 °C. This is an expected outcome as the material thermally transforms from the initial amorphous state (at 1100 °C) to a crystalline state (at ~1400 °C), but further conversion beyond 1400 °C became gentle afterward since a margin of the complete crystallization may have been attained around 1400 °C [49,50].

The inter-defect distance ( $L_D$ ), average continuous graphene length including tortuosity ( $L_{eq}$ ) and defect density ( $\eta_D$ ) were calculated using Equation (2) [51], Equation (3) [52] and Equation (4) [44] respectively (where  $\lambda_L$  is 514 nm). The inter-defect distance,  $L_D$ , and relatively defect density,  $\eta_D$  of the samples also show dependence on the annealing temperature with which the monoliths were produced. An increase in the inter-defect distance of the  $sp^2$  hybridized carbon structure as annealing temperature increases invariably led to the corresponding reduction in the defect densities,  $\eta_D$  (see Figure 2c). The surge in  $L_D$  could be attributed to the progressive  $sp^3$  to  $sp^2$  conversion and indeed ordering of the graphitic structure noticed between  $1100\text{ °C} \leq T \leq 1600\text{ °C}$ . Meanwhile, the recorded inter-defect distance on the C/SiCN nanocomposites in this study is higher when compared with C/SiOC PDCs produced under similar temperature conditions [46,53]. The  $L_D$  values are also more favourable than other polymer-derived SiCN materials found in the literature –although the recently proposed Cancado equation was not adopted in the studies [44,45,54,55]. This shows that the carbon-rich SiCN materials contain minimum defects and this could be associated with the fabrication parameters used in the production of the sample series.

$$L_D = \sqrt{(1.8 \times 10^{-9}) \lambda_L^4 \left(\frac{A_G}{A_D}\right)} \quad (2)$$

$$L_{eq} = 33.6343 \left(\frac{A_{2D}}{A_D}\right) \quad (3)$$

$$\eta_D = \frac{2.4 \times 10^{22}}{\lambda_L^4} \left(\frac{A_D}{A_G}\right) \quad (4)$$

Accordingly, the average continuous graphene length including tortuosity ( $L_{eq}$ ) increased with an increase in crystallite size ( $L_a$ ) as shown in Figure 2d. This outcome may be correlated with the increase in electrical conductivity noticed in the synthesized materials across the increase in annealing temperature as discussed in Section 3.3.

Notice that the 2D band (see Figure 1a–c) becomes more and more pronounced as the thermal treatment of the monoliths tends toward 1600 °C. Information on the stacking number of graphene layers,  $L_c$ , was examined using G and 2D band shape profiles [56]. The 2D band is an overtone of the D band revealed through vibrations from the intrinsic defect-free graphitic  $sp^2$  hybridized carbon structures and it provides knowledge of the number of graphene layers. According to Wall, the value of  $I_{2D}/I_G$  ratio for high-quality, defect-free single-layer graphene will be equal to 2nm [57]. As shown in Table 1,  $I_{2D}/I_G$  ratio of the monoliths is 1.7 nm at all tested temperatures, revealing the presence of single to three layers-graphene within the material. Besides, it has been reported that during thermal decomposition of SiCN, the  $sp^2$  hybridized carbon forms Basic Structural Units (BSUs) which are the first phase to nucleate in about 2 or 3 stack of graphene layers piled up in graphitic arrangements [58].

### 3.2. Crystallization and Stoichiometry

As reported earlier, only SiC and  $sp^2$  hybridized carbon are the electrically conducting components of the C/SiCN (having SiC/Si<sub>3</sub>N<sub>4</sub>/C nanodomains) as Si<sub>3</sub>N<sub>4</sub> does not conduct electricity but provides structural stability [38]. The crystallization of the carbon-rich

SiCN is evaluated using XRD. The X-ray diffraction pattern confirms that the material is amorphous at 1100 °C as no reflections were shown at this temperature (Figure 3). However, reflections indicating the crystallization of the samples were revealed at  $T \geq 1400$  °C and assigned to the  $\beta$ -SiC (F-43m, Pearson symbol: cF8) as the major crystalline phase with traces of stacking faults (SF) [59–61]. Further investigation of the normalized diffraction intensities reveals that as the temperature increases from 1400 °C to 1600 °C, the stacking fault (SF) in the  $\beta$ -SiC becomes healed or suppressed by over 50%. This observation could be linked to the rising stability of beta-SiC with the temperature increase.

**Table 1.** The carbon phase structure of the carbon-rich SiCN materials.

Parameter/Temperature	1100 °C	1400 °C	1600 °C
Lateral crystallite size, $L_a$ (nm)	7.66	8.54	10.08
Average continuous graphene length including tortuosity, $L_{eq}$ (nm)	11.06	15.91	17.76
Inter-defect distance, $L_D$ (nm)	7.58	8.00	8.69
Defect density, $n_D, \times 10^{11}(\text{cm}^{-2})$	7.52	6.75	5.71
$I_{2D}/I_G$ ratio, i.e., stacking number of graphene layer, $L_c$ (nm)	1.7 ( $\leq 3$ layers)	1.7 ( $\leq 3$ layers)	1.7 ( $\leq 3$ layers)

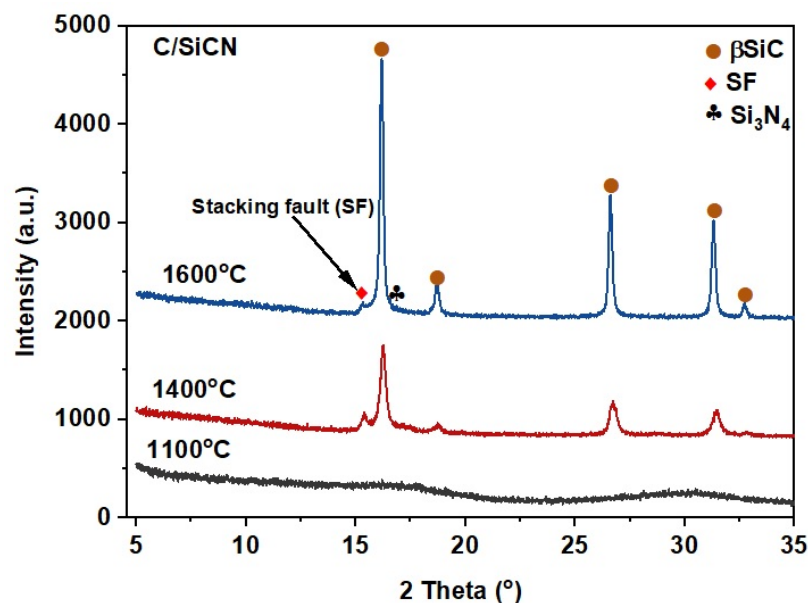


**Figure 3.** An XRD pattern of the C/SiCN monoliths fabricated at different temperatures.

$\beta$ -SiC have been widely investigated as semiconductors for applications in microelectromechanical systems (MEMS) [62–64]. Electrical conductivity in graphitic PDC materials has however been attributed to the percolation network of the free carbon (as long as the C to Si ratio is  $\geq 0.7$ ) [58]. The dominating character of free carbon on the electrical properties of the carbon rich SiCN materials could be traced to its high conductivity of  $1\text{--}10^5$  (S/cm) compared with the conductivity of SiC which is within the range of  $10^{-4}\text{--}10^2$  (S/cm) [14]. This, however, depends on composition and processing conditions that could promote change in hybridization of the carbon atom for sufficient  $sp^3$  to  $sp^2$  transformation as pyrolysis temperature is increased [33]. SiC has been described as a compound semiconductor with a wide bandgap and several advantages over silicon [65]. Hole carrier mobility in SiC polytypes is very small and the majority of the carrier concentration are electrons for the fabrication of n-type semiconductors [66]. In a recent report, Chen et al. divulged the need to account for the relationship between the conductivity of the free carbon and that of the Si-C-N in materials [13]. Kim et al. equally reported the possibility of the notable contribution of (SiOC PDC precipitated) nano-crystalline SiC grains to the overall electrical properties [67]. In essence, the carrier transport mechanism in polycrystalline materials may

be better understood by evaluating the contribution of individual components available for electrical conduction and the impurities available as dopant. Therefore, electron-dominated carrier transport resulting in the n-type semiconductors may be possible in SiCN materials with very low  $sp^2$  carbon content or high amorphous carbon ( $sp^3$  carbon). However, the synthesized C/SiCN nanocomposites demonstrated hole-dominated carrier transport of p-type semiconductors, occasioned by the ordering of the  $sp^2$  carbon induced via the thermal treatments but showed electron-dominated n-type semiconductor at 1100 °C (see Section 3.3 for further details).

The elemental composition was determined using Energy Dispersive X-ray Spectroscopy, EDX, attached to a (High Resolution) Scanning Electron Microscopy (SEM). SEM images showing the morphologies as well as the EDS spectra revealing the energy peaks corresponding to the various elements identified in the carbon-rich SiCN samples are shown in Figure 4a–c. The formation of microcracks was noticed on the surface of the samples, while the wide distribution of dark spots across the morphologies attest to the high amount of graphitic carbon in the samples (see Figure 4ai,bi,ci). The amorphous C/SiCN material prepared at 1100 °C contains ca. 64 at. % carbon with traces of oxygen (1.86 at. %). However, the traces of oxygen at  $T = 1600$  °C have reduced to 0.59 at. % with ca. 72 at. % carbon as shown in Table 2. Typically, oxygen is present as small silica domains in these materials—at high temperatures, these react with  $sp^2$  carbon to form beta-SiC and lead to CO gas release [68,69]. Moreover, a recent study by Haluschka et. al., reported that at annealing temperature of 1400 °C–1600 °C, outgassing of  $N_2$  leading to a decrease in nitrogen content and increase in both silicon and carbon content may occur (although only nitrogen atmosphere was considered in the study as against the argon atmosphere adopted in this study) [33].

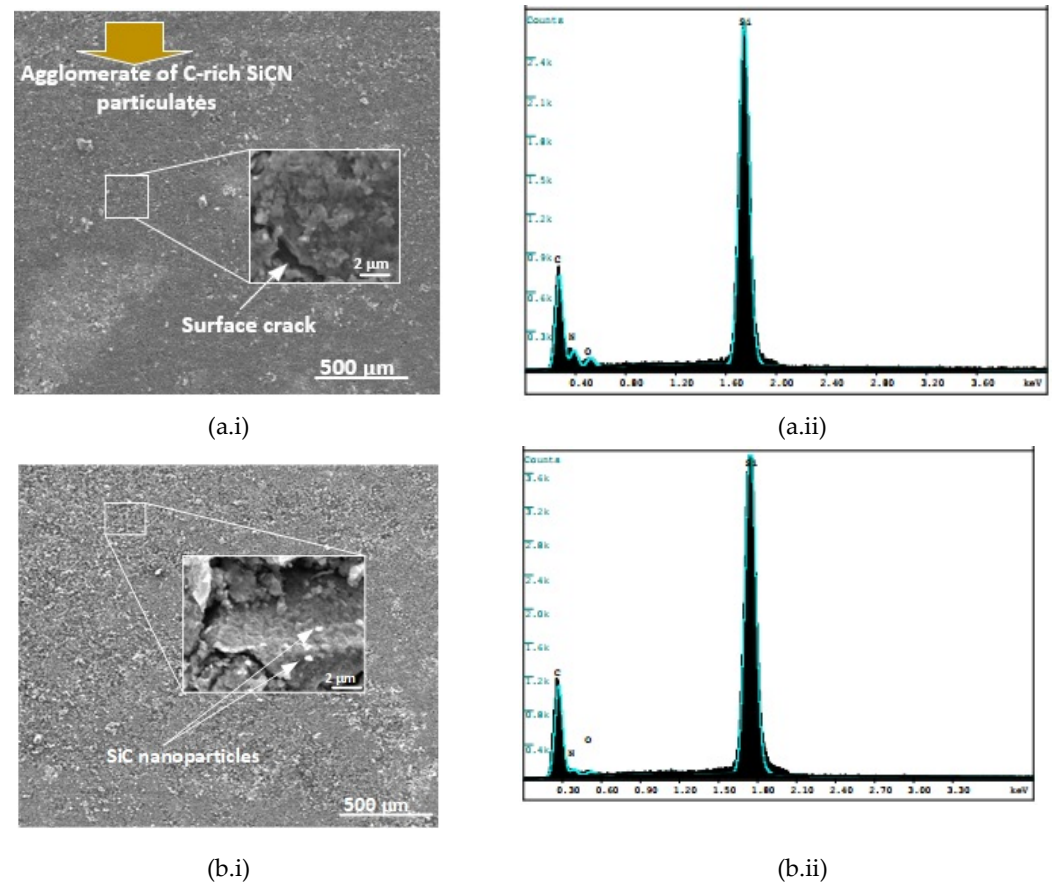
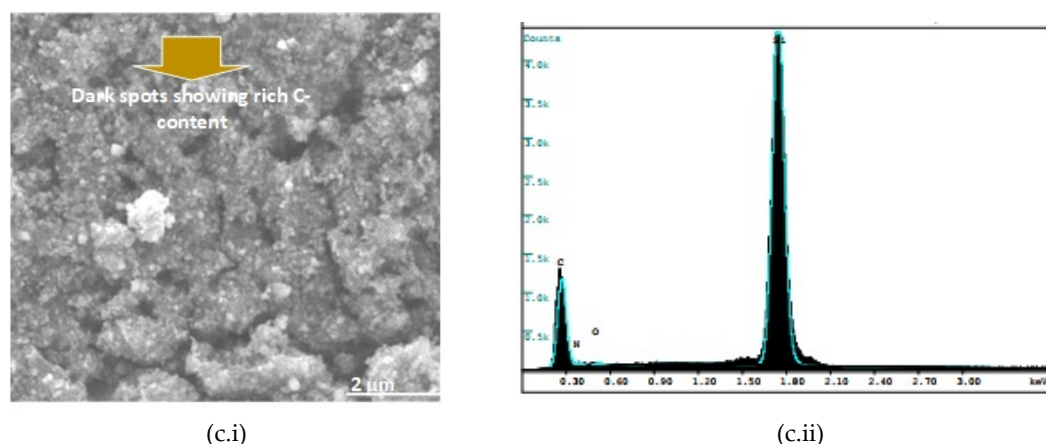


Figure 4. Cont.



**Figure 4.** SEM images and EDS spectra showing the morphologies and energy peaks corresponding to the various elements respectively, of the pelletized C/SiCN nanocomposites pyrolyzed and heat treated between 1100–1600 °C in an argon atmosphere: (a.i) SEM images of the samples pyrolyzed at 1100 °C; (a.ii) EDS spectrum of the sample pyrolyzed at 1100 °C; (b.i) SEM images of the samples heat treated at 1400 °C; (b.ii) EDS spectrum of the sample heat treated at 1400 °C; (c.i) SEM images of the samples heat treated at 1600 °C; (c.ii) EDS spectrum of the sample heat treated at 1600 °C.

**Table 2.** The chemical composition of the C/SiCN nanocomposites after pyrolysis.

Pyrolysis Temperature	Elemental Composition (wt. %)			N/Si (at. %)	C/Si (at. %)	Carbon Content (at. %)
	Si	C	N			
1100 °C	39.87	48.32	9.95	0.50	2.83	64.17
1400 °C	41.91	52.87	4.44	0.21	2.95	70.32
1600 °C	43.61	53.37	2.43	0.11	2.86	71.60

### 3.3. Room Temperature Electrical Conductivity and Charge Carrier Transport Mechanism

The room temperature conductivity of the amorphous carbon-rich SiCN produced at pyrolysis temperature of 1100 °C (in an argon atmosphere) was determined to be  $1.48 \times 10^{-1}$  S/cm (see Table 3). This result is concurrent with the submission of Cordelair that amorphous  $\text{Si}_x\text{C}_y\text{N}_z$  is a semiconductor with room temperature dc conductivity in the range of  $10^{-4}$  to  $10^2$  S/cm [14]. However, this value is found to be at least 3 orders of magnitude higher than previously reported electrical conductivity of amorphous SiCN PDC materials prepared under similar temperature conditions [13,70]. The higher electrical conductivity recorded could be traced to the higher free carbon content. Various models governing the dependence of electrical properties of SiCN on fabrication pyrolysis temperature have been proposed [71–75], but electrical conductivity ( $\sigma_{dc}$ ) dependence on temperature of amorphous semiconductors can best be described by variable range hopping of charge carriers (i.e., single/multiple phonon-assisted jumps of charge carriers near the Fermi level) described by Mott (Equation (5)) [74,75] ( $k$  is Boltzmann constant,  $\Delta E$  is the activation energy which equals the energy gap between Fermi level and conducting bands). Also, it has been shown that at higher temperatures (e.g.,  $T \geq 1400$  °C for SiCN PDCs), Arrhenius equation (see Equation (6)) describes temperature dependence of the RT  $\sigma_{dc}$  [9,14,76].

$$\sigma_{dc} = \sigma_o \exp - \left( \frac{T_o}{T} \right)^{\frac{1}{4}} \quad (5)$$

$$\sigma_{dc} = \sigma_o \exp - \left( \frac{\Delta E}{kT} \right) \quad (6)$$

**Table 3.** Electrical properties of the carbon-rich SiCN materials.

Parameter/Temperature	1100 °C	1400 °C	1600 °C
Electrical conductivity $\sigma_{dc}$ , (S/cm)	0.148	4.71	9.26
Carrier density, $N$ ( $\text{cm}^{-3}$ )	$6.42 \times 10^{18}$	$8.45 \times 10^{19}$	$1.63 \times 10^{19}$
Carrier mobility, $\mu_H$ , ( $\text{cm}^2 \text{V}^{-1} \text{s}^{-1}$ )	$1.45 \times 10^{-1}$	$3.52 \times 10^{-1}$	3.55

Consequently, the RT conductivity of the samples prepared at an annealing temperature of 1400 °C increased to 4.70 S/cm and 9.26 S/cm at to 1600 °C. The noticed surge in electrical conductivity of the C/SiCN materials is attributed to the percolation and ordering of the graphitic domains with increasing the annealing temperature. A demanding search of the literature shows that the highest electrical conductivity of SiCN monolith so far reported is ~1.0 S/cm (at 1700 °C) [9], but the conductivity value recorded on the synthesized C/SiCN nanocomposite in this study heat-treated at 1600 °C is much higher (9.26 S/cm); revealing the extent to which the temperature-dependent electrical properties of PDCs may be tailored corresponding to increase in the quantity and ordering of the free carbon.

The electrical properties of the C/SiCN nanocomposites investigated using Hall measurement showed an anomalous shift in the majority charge carriers from n-type in the glassy matrix pyrolyzed at 1100 °C to p-type in the ceramic samples prepared at  $T \geq 1400$  °C (see Figure 5a–c). Recall that evaluation of the crystallization of the carbon-rich SiCN samples supported using XRD indicates that the material is amorphous at 1100 °C and crystalline at  $T \geq 1400$  °C (Figure 3). Besides, phase composition of the amorphous SiC(N) is comparable to that of SiC doped with nitrogen [9]. Nitrogen dopant is commonly used for producing n-type SiC semiconductors [77,78]. In the amorphous state, therefore, the transport mechanism of the carbon-rich SiCN samples appears to behave similar to that of SiC doped with nitrogen by showing predominant n-type charge carriers. Moreover, the presence of nitrogen doped SiC in SiCN PDCs pyrolyzed in nitrogen atmosphere has been recently reported, corroborated with results obtained using TEM, XANES-spectroscopy, XRD and Raman-spectroscopy [9]. In addition, it is known that  $sp^3$  carbon is a good electron insulator while  $sp^2$  carbon is an excellent charge transmitter [79], and as shown earlier in Figure 1a (by the prominence of the D' and T Raman bands), the pre-eminence of the insulating  $sp^3$  carbon can be seen in the amorphous C/SiCN sample at 1100 °C. This may have led to the low carrier mobility and conductivity recorded at the 1100 °C temperature (see Table 3). On the other hand, the crystalline carbon-rich SiCN semiconductors produced at pyrolysis temperatures of 1400 °C and 1600 °C show a change in the predominant charge carrier to p-type. The nature of graphitic carbon charge carriers has been previously described as a reproducible positive Hall coefficient signal of hole-dominated transport (p-type) [80], and the p-type carriers shown by the C/SiCN PDCs could be linked to the prevailing ordering and percolation network of the graphitic phase within the nanocomposites at the higher temperatures. The progressive ordering, amount and size of the  $sp^2$  carbon at 1400 °C and 1600 °C can be confirmed by the consistent increase in the lateral crystallite size ( $L_a$ ), as well as the average continuous graphene length including tortuosity ( $L_{eq}$ ) as the pyrolysis temperature increases. Furthermore, between 1100 °C and  $1400 \text{ °C} \leq T \leq 1600 \text{ °C}$ , the  $sp^3$  to  $sp^2$  conversion is revealed via puniness of the D' and T Raman bands (see Figure 1b,c), leading to corresponding increases in the carrier mobility and electrical conductivity (Table 3), as well as the percolation network of the free carbon within the nanocomposites to display the recorded shift from the n-type to a p-type semiconductor.

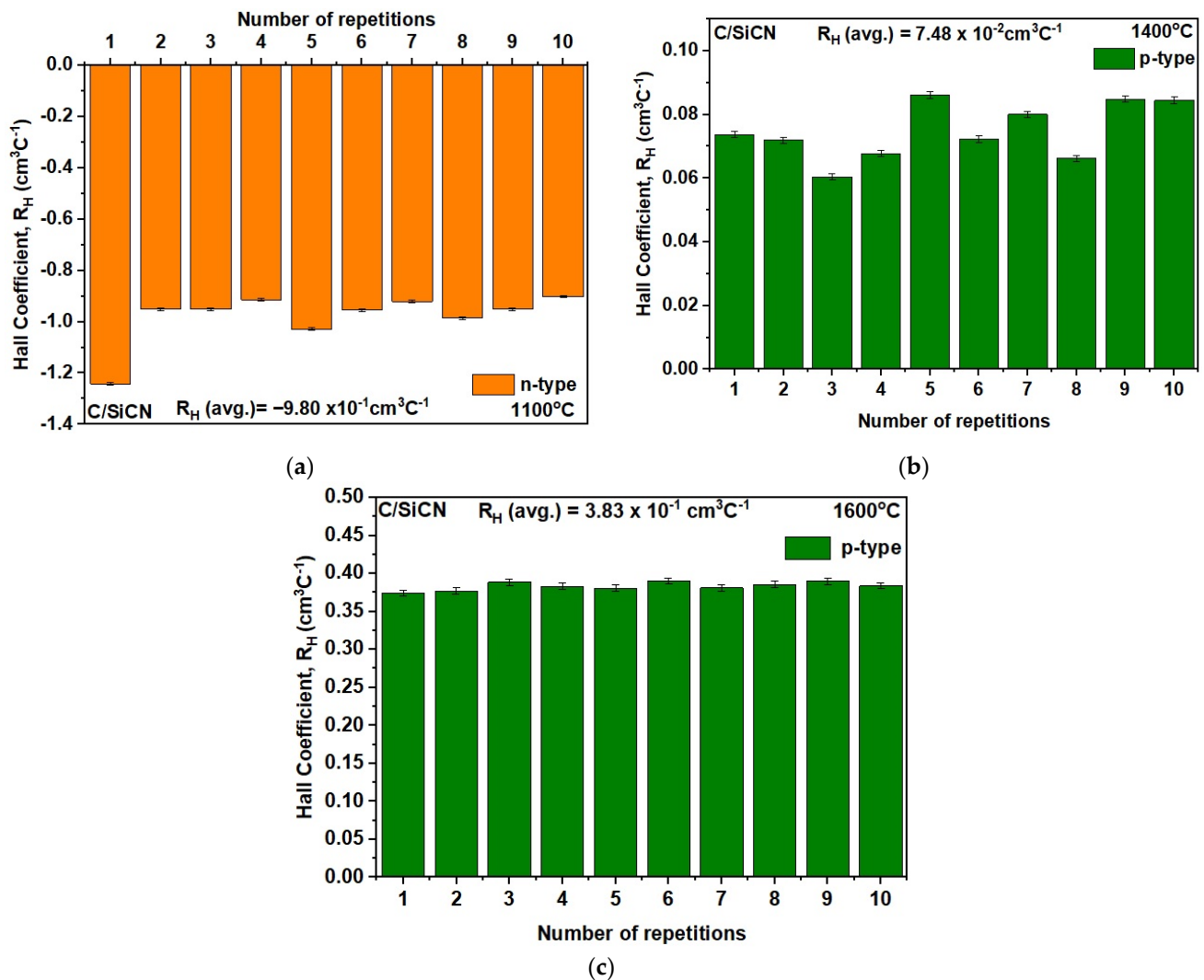


**Figure 5.** Hall measurement performed in 10 repetitions on the C/SiCN nanocomposites showing the shift in predominant charge carriers from n-type at 1100 °C to p-type at higher temperatures  $\geq 1400$  °C: (a) Hall coefficients at 1100 °C showing n-type carriers; (b) Hall coefficients of the sample prepared at 1400 °C showing p-type carriers; (c) Hall coefficients of the carbon rich SiCN prepared at 1600 °C showing p-type carriers.

#### 4. Conclusions

The structure and electronic properties of carbon-rich polymer-derived SiCN (up to ca. 72 at. % carbon) heat-treated in an argon atmosphere at 1100–1600 °C are herein investigated and reported. The electrical properties of the C/SiCN nanocomposites examined using Hall measurement demonstrated an anomalous change in the majority charge carriers from n-type in the samples pyrolyzed at 1100 °C to p-type in the samples prepared at  $T \geq 1400$  °C. Moreover, it was found that RT conductivity of the materials produced at 1000–1600 °C increased from 0.148 S/cm to 9.26 S/cm which are much higher than the previously reported values for monolith samples produced using similar pyrolysis and annealing temperature. Both the anomalous shift in predominant carriers and high electrical conductivities are attributed to the preliminary quantity of carbon content and evolution of the  $\text{sp}^3$  to  $\text{sp}^2$  hybridized carbon transformation as the processing temperature increases. Furthermore, parameters associated with the  $\text{sp}^3$  to  $\text{sp}^2$  transition in the carbon-rich SiCN structure investigated using Raman spectroscopy such as: the crystallite size ( $L_a$ ), average continuous graphene length including tortuosity ( $L_{eq}$ ), and inter-defect distance ( $L_D$ ) all increased with an increase in processing temperatures. Interestingly, the stacking

number of graphene layers ( $L_c$ ) of the graphitic carbon phase was found to contain mono to three layers of graphene across all adopted processing temperatures. Depending on the phase composition and processing conditions, custom-made carbon-rich SiCN polymer-derived ceramics could be developed to produce n-type and p-type semiconductors for the development of the future generation of micro-electromechanical systems (MEMS), heterojunction diodes and other electronic devices for applications in extremely high temperature environments.

**Author Contributions:** Conceptualization, O.D.A. and E.I.; Formal analysis, O.D.A.; Investigation, O.D.A.; Methodology, O.D.A., E.R.III and E.I.; Resources, E.I.; Supervision, A.A.D., L.E.U. and E.I.; Writing—original draft, O.D.A.; Writing—review & editing, O.D.A., E.R.III, A.A.D., L.E.U. and E.I. All authors have read and agreed to the published version of the manuscript.

**Funding:** Financial support from the Tertiary Education Trust Fund, TETFUND towards the success of the experiment is acknowledged and duly appreciated.

**Institutional Review Board Statement:** Not applicable.

**Informed Consent Statement:** Not applicable.

**Data Availability Statement:** Not applicable.

**Conflicts of Interest:** The authors declare no conflict of interest.

## References

1. Barrios, E.; Zhai, L. A review of the evolution of the nanostructure of SiCN and SiOC polymer derived ceramics and the impact on mechanical properties. *Mol. Syst. Des. Eng.* **2020**, *5*, 1606–1641. [[CrossRef](#)]
2. Shen, C.; Calderon, J.E.; Barrios, E.; Soliman, M.; Khater, A.; Jeyaranjan, A.; Tetard, L.; Gordon, A.; Seal, S.; Zhai, L. Anisotropic electrical conductivity in polymer derived ceramics induced by graphene aerogels. *J. Mater. Chem. C* **2017**, *5*, 11708–11716. [[CrossRef](#)]
3. Niu, J.; Meng, S.; Jin, H.; Yi, F.; Li, J.; Zhang, G.; Zhou, Y. Electrical conductivity change induced by porosity within polymer-derived SiCN ceramics. *J. Alloys Compd.* **2019**, *777*, 1010–1016. [[CrossRef](#)]
4. Francis, A. Progress in polymer-derived functional silicon-based ceramic composites for biomedical and engineering applications. *Mater. Res. Express* **2018**, *5*, 6. [[CrossRef](#)]
5. Ren, Z.; Mujib, S.B.; Singh, G. High-temperature properties and applications of Si-based polymer-derived ceramics: A review. *Materials* **2021**, *14*, 614. [[CrossRef](#)]
6. Ting, S.; Fang, Y.; Hsieh, W.; Tsair, Y.; Chang, C.; Lin, C. A High Breakdown-Voltage SiCN/Si Heterojunction. *IEEE Electron Device Lett.* **2002**, *23*, 142–144. [[CrossRef](#)]
7. Chowdhury, M.A.R.; Wang, K.; Jia, Y.; Xu, C. Electrical conductivity and structural evolution of polymer-derived SiC ceramics pyrolyzed from 1200 °C to 1800 °C. *J. Micro Nano-Manuf.* **2020**, *8*, 024502. [[CrossRef](#)]
8. Chen, L.C.; Chen, C.K.; Wei, S.L.; Bhusari, D.M.; Chen, K.H.; Chen, Y.F.; Jong, Y.C.; Huang, Y.S. Crystalline silicon carbon nitride: A wide band gap semiconductor. *Appl. Phys. Lett.* **1998**, *72*, 2463–2465. [[CrossRef](#)]
9. Haluschka, C.; Engel, C.; Riedel, R. Silicon carbonitride ceramics derived from polysilazanes Part II. Investigation of electrical properties. *J. Eur. Ceram. Soc.* **2000**, *20*, 1365–1374. [[CrossRef](#)]
10. Heidenreich, B. C/SiC and C/C-SiC Composites. In *Ceramic Matrix Composites: Materials, Modeling and Technology*; The American Ceramic Society: Westerville, OH, USA, 2014; pp. 147–216. [[CrossRef](#)]
11. Boden, G.; Neumann, A.; Breuning, T.; Tschernikova, E.; Hermel, W. Nanosized Si-C-N-powders by polysilazane pyrolysis and Si<sub>3</sub>N<sub>4</sub>/SiC-composite materials thereof. *J. Eur. Ceram. Soc.* **1998**, *18*, 1461–1469. [[CrossRef](#)]
12. Kleebe, H.-J.; Störmer, H.; Trassl, S.; Ziegler, G. Thermal stability of SiCN ceramics studied by spectroscopy and electron microscopy. *Appl. Organomet. Chem.* **2001**, *15*, 858–866. [[CrossRef](#)]
13. Chen, Y.; Yang, F.; An, L. On electric conduction of amorphous silicon carbonitride derived from a polymeric precursor. *Appl. Phys. Lett.* **2013**, *102*, 231902. [[CrossRef](#)]
14. Cordelair, J.; Greil, P. Electrical conductivity measurements as a microprobe for structure transitions in polysiloxane derived Si-O-C ceramics. *J. Eur. Ceram. Soc.* **2000**, *20*, 1947–1957. [[CrossRef](#)]
15. Iyer, R.; Kousaalya, A.B.; Pilla, S. Polymer-derived ceramics: A novel inorganic thermoelectric material system. In *Novel Thermoelectric Materials and Device Design Concepts*; Springer: Berlin/Heidelberg, Germany, 2019; pp. 229–252.
16. Ryu, H.Y.; Wang, Q.; Raj, R. Ultrahigh-temperature semiconductors made from polymer-derived ceramics. *J. Am. Ceram. Soc.* **2010**, *93*, 1668–1676. [[CrossRef](#)]
17. Mocaer, D.; Pailler, R.; Naslain, R.; Richard, C.; Pillot, J.P.; Dunogues, J.; Gerardin, C.; Taulelle, F. Si-C-N ceramics with a high microstructural stability elaborated from the pyrolysis of new polycarbosilazane precursors—Part III Effect of pyrolysis conditions on the nature and properties of oxygen-cured derived monofilaments. *J. Mater. Sci.* **1993**, *28*, 2639–2653. [[CrossRef](#)]

18. Ellmer, K. Hall Effect and Conductivity Measurements in Semiconductor Crystals and Thin Films. In *Characterization of Materials*; John Wiley & Sons, Inc.: Hoboken, NJ, USA, 2012; pp. 1–16. [CrossRef]
19. Kinder, R.; Mikolášek, M.; Donoval, D.; Kováč, J.; Tlaczala, M. Measurement System with Hall and a Four Point Probes for Characterization of Semiconductors. *J. Electr. Eng.* **2013**, *64*, 106–111. [CrossRef]
20. Sultana, M. Research Gate. Re: Why Hall Coefficient Vary from Positive to Negative Randomly for the Same Sample at Same Condition? Available online: <https://www.researchgate.net/post/Why-Hall-Coefficient-vary-from-positive-to-negative-randomly-for-the-same-sample-at-same-condition/59d9b276615e27ec58463d1e/citation/download> (accessed on 25 March 2022).
21. Usama, H. Research Gate. Re: Why Hall Effect Measurement Giving Wrong Values? Available online: [https://www.researchgate.net/post/Why\\_Hall\\_effect\\_measurement\\_giving\\_wrong\\_values/59120db9cbd5c294a1716722/citation/download](https://www.researchgate.net/post/Why_Hall_effect_measurement_giving_wrong_values/59120db9cbd5c294a1716722/citation/download) (accessed on 29 March 2022).
22. Hermann, A.M.; Wang, Y.T.; Ramakrishnan, P.A.; Balzar, D.; An, L.; Haluschka, C.; Riedel, R. Structure and Electronic Transport Properties of Si-(B)-C-N Ceramics. *J. Am. Ceram. Soc.* **2001**, *84*, 2260–2264. [CrossRef]
23. Widgeon, S.; Mera, G.; Gao, Y.; Stoyanov, E.; Sen, S.; Navrotsky, A.; Riedel, R. Nanostructure and energetics of carbon-rich SiCN ceramics derived from polysilylcarbodiimides: Role of the nanodomain interfaces. *Chem. Mater.* **2012**, *24*, 1181–1191. [CrossRef]
24. Rosenburg, F.; Balke, B.; Nicoloso, N.; Riedel, R.; Ionescu, E. Effect of the Content and Ordering of the sp<sup>2</sup> Free Carbon Phase on the Charge Carrier Transport in Polymer-Derived Silicon Oxycarbides. *Molecules* **2020**, *25*, 5919. [CrossRef]
25. Sorarù, G.D.; Kundanati, L.; Santhosh, B.; Pugno, N. Influence of free carbon on the Young's modulus and hardness of polymer-derived silicon oxycarbide glasses. *J. Am. Ceram. Soc.* **2019**, *102*, 907–913. [CrossRef]
26. Dalcanale, F.; Grossenbacher, J.; Blugan, G.; Gullo, M.R.; Lauria, A.; Brugger, J.; Tevæarai, H.; Graule, T.; Niederberger, M.; Kuebler, J. Influence of carbon enrichment on electrical conductivity and processing of polycarbosilane derived ceramic for MEMS applications. *J. Eur. Ceram. Soc.* **2014**, *34*, 3559–3570. [CrossRef]
27. Drechsel, C.; Peterlik, H.; Gierl-Mayer, C.; Stöger-Pollach, M.; Konegger, T. Influence of DVB as linker molecule on the micropore formation in polymer-derived SiCN ceramics. *J. Eur. Ceram. Soc.* **2021**, *41*, 3292–3302. [CrossRef]
28. Chen, Y.; Li, C.; Wang, Y.; Zhang, Q.; Xu, C.; Wei, B.; An, L. Self-assembled carbon-silicon carbonitride nanocomposites: High-performance anode materials for lithium-ion batteries. *J. Mater. Chem.* **2011**, *21*, 18186–18190. [CrossRef]
29. Hanniet, Q.; Boussmen, M.; Barés, J.; Huon, V.; Iatsunskiy, I.; Coy, E.; Bechelany, M.; Gervais, C.; Voiry, D.; Miele, P.; et al. Investigation of polymer-derived Si-(B)-C-N ceramic/reduced graphene oxide composite systems as active catalysts towards the hydrogen evolution reaction. *Sci. Rep.* **2020**, *10*, 22003. [CrossRef] [PubMed]
30. Qu, F.; Yu, Z.; Krol, M.; Chai, N.; Riedel, R.; Graczyk-Zajac, M. Electrochemical Performance of Carbon-Rich Silicon Carbonitride Ceramic as Support for Sulfur Cathode in Lithium Sulfur Battery. *Nanomaterials* **2022**, *12*, 1283. [CrossRef] [PubMed]
31. Mujib, S.B.; Ribot, F.; Gervais, C.; Singh, G. Self-supporting carbon-rich SiOC ceramic electrodes for lithium-ion batteries and aqueous supercapacitors. *RSC Adv.* **2021**, *11*, 35440–35454. [CrossRef]
32. Riedel, R.; Seher, M.; Mayer, J.; Szabó, D.V. Polymer-derived Si-based bulk ceramics, part I: Preparation, processing and properties. *J. Eur. Ceram. Soc.* **1995**, *15*, 703–715. [CrossRef]
33. Haluschka, C.; Kleebe, H.J.; Franke, R.; Riedel, R. Silicon carbonitride ceramics derived from polysilazanes Part I. Investigation of compositional and structural properties. *J. Eur. Ceram. Soc.* **2000**, *20*, 1355–1364. [CrossRef]
34. Ricohermoso, E.; Klug, F.; Schlaak, H.; Riedel, R.; Ionescu, E. Compressive thermal stress and microstructure-driven charge carrier transport in silicon oxycarbide thin films. *J. Eur. Ceram. Soc.* **2021**, *41*, 6377–6384. [CrossRef]
35. Flores, O.; Bordia, R.K.; Bernard, S.; Uhlemann, T.; Krenkel, W.; Motz, G. Processing and characterization of large diameter ceramic SiCN monofilaments from commercial oligosilazanes. *RSC Adv.* **2015**, *5*, 107001–107011. [CrossRef]
36. Yuan, W.; Qu, L.; Li, J.; Deng, C.; Zhu, H. Characterization of crystalline SiCN formed during the nitridation of silicon and cornstarch powder compacts. *J. Alloys Compd.* **2017**, *725*, 326–333. [CrossRef]
37. Khatami, Z.; Wilson, P.R.J.; Wojcik, J.; Mascher, P. The influence of carbon on the structure and photoluminescence of amorphous silicon carbonitride thin films. *Thin Solid Films* **2017**, *622*, 1–10. [CrossRef]
38. Wen, Q.; Yu, Z.; Riedel, R. The fate and role of in situ formed carbon in polymer-derived ceramics. *Prog. Mater. Sci.* **2020**, *109*, 100623. [CrossRef]
39. Mera, G.; Navrotsky, A.; Sen, S.; Kleebe, H.-J.; Riedel, R. Polymer-derived SiCN and SiOC ceramics—Structure and energetics at the nanoscale. *J. Mater. Chem. A* **2013**, *1*, 3826–3836. [CrossRef]
40. Wilamowska, M.; Graczyk-Zajac, M.; Riedel, R. Composite materials based on polymer-derived SiCN ceramic and disordered hard carbons as anodes for lithium-ion batteries. *J. Power Sources* **2013**, *244*, 80–86. [CrossRef]
41. Li, M.; Cheng, L.; Ye, F.; Zhang, C.; Zhou, J. Formation of nanocrystalline graphite in polymer-derived SiCN by polymer infiltration and pyrolysis at a low temperature. *J. Adv. Ceram.* **2021**, *10*, 1256–1272. [CrossRef]
42. Ferrari, A.C. Raman spectroscopy of graphene and graphite: Disorder, electron-phonon coupling, doping and nonadiabatic effects. *Solid State Commun.* **2007**, *143*, 47–57. [CrossRef]
43. Ferrari, A.C.; Robertson, J. Interpretation of Raman spectra of disordered and amorphous carbon. *Am. Phys. Soc.* **2000**, *61*, 95–107. [CrossRef]
44. Cançado, L.G.; Jorio, A.; Ferreira, E.M.; Stavale, F.; Achete, C.A.; Capaz, R.B.; Moutinho, M.V.D.O.; Lombardo, A.; Kulmala, T.S.; Ferrari, A.C. Quantifying defects in graphene via Raman spectroscopy at different excitation energies. *Nano Lett.* **2011**, *11*, 3190–3196. [CrossRef]

45. Cançado, L.G.; Takai, K.; Enoki, T.; Endo, M.; Kim, Y.A.; Mizusaki, H.; Jorio, A.; Coelho, L.N.; Magalhães-Paniago, R.; Pimenta, M.A. General equation for the determination of the crystallite size  $l_a$  of nanographite by Raman spectroscopy. *Appl. Phys. Lett.* **2006**, *88*, 163106. [CrossRef]
46. Ricohermoso, E.I.I.I.; Klug, F.; Schlaak, H.; Riedel, R.; Ionescu, E. Electrically conductive silicon oxycarbide thin films prepared from preceramic polymers. *Int. J. Appl. Ceram. Technol.* **2022**, *19*, 149–164. [CrossRef]
47. Zhao, M.; Xiong, D.B.; Tan, Z.; Fan, G.; Guo, Q.; Guo, C.; Li, Z.; Zhang, D. Lateral size effect of graphene on mechanical properties of aluminum matrix nanolaminated composites. *Scr. Mater.* **2017**, *139*, 44–48. [CrossRef]
48. Tarhini, A.; Tehrani-Bagha, A.; Kazan, M.; Grady, B. The effect of graphene flake size on the properties of graphene-based polymer composite films. *J. Appl. Polym. Sci.* **2021**, *38*, 49821. [CrossRef]
49. Ferrari, A.; Robertson, J. Interpretation of Raman spectra of disordered and amorphous carbon. *Phys. Rev.* **2000**, *61*, 14095–14107. [CrossRef]
50. Pelletier, M.J. Quantitative Analysis Using Raman Spectrometry. *Appl. Spectrosc.* **2003**, *57*, 20A–42A. [CrossRef] [PubMed]
51. Pimenta, M.A.; Dresselhaus, G.; Dresselhaus, M.S.; Cançado, L.G.; Jorio, A.; Saito, R. Studying disorder in graphite-based systems by Raman spectroscopy. *Phys. Chem. Chem. Phys.* **2007**, *9*, 1276–1291. [CrossRef]
52. Larouche, N.; Stansfield, B.L. Classifying nanostructured carbons using graphitic indices derived from Raman spectra. *Carbon* **2009**, *48*, 620–629. [CrossRef]
53. Stabler, C.; Reitz, A.; Stein, P.; Albert, B.; Riedel, R.; Ionescu, E. Thermal properties of SiOC glasses and glass ceramics at elevated temperatures. *Materials* **2018**, *11*, 279. [CrossRef]
54. Mera, G.; Riedel, R.; Poli, F.; Müller, K. Carbon-rich SiCN ceramics derived from phenyl-containing poly(silylcarbodiimides). *J. Eur. Ceram. Soc.* **2009**, *29*, 2873–2883. [CrossRef]
55. Gao, Y.; Mera, G.; Nguyen, H.; Morita, K.; Kleebe, H.J.; Riedel, R. Processing route dramatically influencing the nanostructure of carbon-rich SiCN and SiBCN polymer-derived ceramics. Part I: Low temperature thermal transformation. *J. Eur. Ceram. Soc.* **2012**, *32*, 1857–1866. [CrossRef]
56. Ionescu, E.; Mera, G.; Riedel, R. Polymer-Derived Ceramics (PDCs): Materials Design towards Applications at Ultrahigh Temperatures and in Extreme Environments. In *MAX Phases and Ultra-High Temperature Ceramics for Extreme Environments*; IGI Global: Hershey, PA, USA, 2013; p. 203. [CrossRef]
57. Wall, M. The Raman Spectroscopy of Graphene and the Determination of Layer Thickness. *Thermo Sci.* **2011**, *5*, 1–5.
58. Monthieux, M.; Delverdier, O. Thermal Behavior of (Organosilicon) Polymer-Derived Ceramics. V: Main Facts and Trends. *J. Eur. Ceram. Soc.* **1996**, *16*, 721–737. [CrossRef]
59. Rivera, J.O.B.; Talou, M.H.; Hung, Y.M.X.H.; Camerucci, M.A. Study of a silicon-based preceramic for the processing of polymer-derived ceramics. *J. Sol-Gel Sci. Technol.* **2019**, *91*, 446–460. [CrossRef]
60. Zhou, C.; Min, H.; Yang, L.; Chen, M.; Wen, Q.; Yu, Z. Dimethylaminoborane-modified copolysilazane as a novel precursor for high-temperature resistant SiBCN ceramics. *J. Eur. Ceram. Soc.* **2014**, *34*, 3579–3589. [CrossRef]
61. Wang, D.H.; Xu, D.; Wang, Q.; Hao, Y.J.; Jin, G.Q.; Guo, X.Y.; Tu, K.N. Periodically twinned SiC nanowires. *Nanotechnology* **2008**, *19*, 215602. [CrossRef]
62. Yao, R.; Feng, Z.; Yu, Y.; Li, S.; Chen, L.; Zhang, Y. Synthesis and characterization of continuous freestanding silicon carbide films with polycarbosilane (PCS). *J. Eur. Ceram. Soc.* **2009**, *29*, 2079–2085. [CrossRef]
63. Wijesundara, M.B.J.; Azevedo, R.G. SiC MEMS devices. In *Silicon Carbide Microsystems for Harsh Environments*; Springer: New York, NY, USA, 2011; pp. 125–165. [CrossRef]
64. Masripah, A. Zulys, and J. Setiawan. Synthesis of Silicon Carbide Fiber as semiconductor substrate for Betavoltaic cell. *J. Phys. Conf. Ser.* **2018**, *1025*, 012129. [CrossRef]
65. ROHM Semiconductor. What are SiC Semiconductors? (SiC) | Electronics Basics. Available online: <https://www.rohm.com/electronics-basics/sic/what-are-sic-semiconductors> (accessed on 23 March 2022).
66. Codreanu, C.; Avram, M.; Carbunescu, E.; Iliescu, E. Comparison of 3C-SiC, 6H-SiC and 4H-SiC MESFETs performances. *Mater. Sci. Semicond. Proc.* **2000**, *3*, 137–142. [CrossRef]
67. Kim, K.J.; Eom, J.H.; Kim, Y.W.; Seo, W.S. Electrical conductivity of dense, bulk silicon-oxycarbide ceramics. *J. Eur. Ceram. Soc.* **2015**, *35*, 1355–1360. [CrossRef]
68. Bahloul, D.; Pereira, M.; Goursat, P. Silicon carbonitride derived from an organometallic precursor: Influence of the microstructure on the oxidation behaviour. *Ceram. Int.* **1992**, *18*, 1–9. [CrossRef]
69. Burns, G.T.; Angelotti, T.P.; Hanneman, L.F.; Chandra, G.; Moore, J.A. Alkyl- and arylsilsesquiazanes: Effect of the R group on polymer degradation and ceramic char composition. *J. Mater. Sci.* **1987**, *22*, 2609–2614. [CrossRef]
70. Ramakrishnan, P.A.; Wang, Y.T.; Balzar, D.; An, L.; Haluschka, C.; Riedel, R.; Hermann, A.M. Silicoboron-carbonitride ceramics: A class of high-temperature, dopable electronic materials. *Appl. Phys. Lett.* **2001**, *78*, 3076–3078. [CrossRef]
71. Godet, C. Hopping model for charge transport in amorphous carbon. *Philos. Mag. B* **2001**, *81*, 205–222. [CrossRef]
72. Godet, C. Variable range hopping revisited: The case of an exponential distribution of localized states. *J. Non. Cryst. Solids* **2002**, *299–302*, 333–338. [CrossRef]
73. Godet, C. Physics of bandtail hopping in disordered carbons. *Diam. Relat. Mater.* **2003**, *12*, 159–165. [CrossRef]
74. Mott, N.F. Conduction in Non-crystalline Materials III. Localized States in a Pseudogap and Near Extremities of Conduction and Valence Bands. *Philos. Mag. Lett.* **1969**, *19*, 835–852. [CrossRef]

75. Mott, N.F.; Davis, E.A. Electronic processes. In Non-Crystalline Materials. *Phys. Today* **1984**, *7*, 34. [[CrossRef](#)]
76. Trassl, S.; Puchinger, M.; Rössler, E.; Ziegler, G. Electrical properties of amorphous SiC<sub>x</sub>N<sub>y</sub>H<sub>z</sub>-ceramics derived from polyvinylsilazane. *J. Eur. Ceram. Soc.* **2003**, *23*, 781–789. [[CrossRef](#)]
77. Taki, Y.; Kitiwan, M.; Katsui, H.; Goto, T. Electrical and thermal properties of nitrogen-doped SiC sintered body. *Funtai Oyobi Fumatsu Yakin/Journal Jpn. Soc. Powder Powder Metall.* **2018**, *65*, 508–512. [[CrossRef](#)]
78. Chauhan, S.S.; Narwariya, P.; Shrivastava, A.K.; Srivastava, P. Electronic and transport properties of nitrogen and boron doped zigzag silicon carbide nanoribbons: First principle study. *Solid State Commun.* **2021**, *338*, 114476. [[CrossRef](#)]
79. Sanjeev, R.; Ravi, R.; Jagannadham, V. Attenuation Effect as a Tool to Explain sp<sup>3</sup> Carbon (–CH<sub>2</sub>–) is a Good Electron Insulator and a sp<sup>2</sup> Carbon (–CH=CH–) is a Good Electron Transmitter: An Undergraduate 1-h Chemistry Classroom Tutorial. *Natl. Acad. Sci. Lett.* **2020**, *43*, 5–8. [[CrossRef](#)]
80. Richter, N.; Hernandez, Y.R.; Schweitzer, S.; Kim, J.S.; Patra, A.K.; Englert, J.; Lieberwirth, I.; Liscio, A.; Palermo, V.; Feng, X.; et al. Robust two-dimensional electronic properties in three-dimensional microstructures of rotationally stacked turbostratic graphene. *Phys. Rev. Appl.* **2017**, *7*, 024022. [[CrossRef](#)]